EXERGY-BASED ANALYSIS OF IRREVERSIBLE LOSSES IN NASA ROTOR 67 BLADE SECTION

J. du Plessis*, P. Kopper*, A. Beck*
* University of Stuttgart, Institute of Aerodynamics and Gasdynamics, Wankelstraße 3, Stuttgart, Germany

Abstract

Transonic compressor rotors rely on strong shocks to achieve the pressure rise required for modern aero-engine performance. The resulting shock–turbulent boundary-layer interaction generates aerodynamic losses and can give rise to low-frequency shock oscillations known as transonic buffet. In this work, a far-field exergy balance is applied to a wall-resolved large-eddy simulation of a 2.5D section of the NASA Rotor 67 transonic compressor, computed using a high-order discontinuous Galerkin approach. The simulation captures the passage shock, shock-induced separation and buffet dynamics, with a dominant oscillation frequency of 489 Hz identified from the blade work coefficient. The balance is evaluated as a post-processing operation and swept through the passage to examine the spatial evolution of energy transfer, and shows that mechanical exergy is the dominant form in which work is delivered to the fluid. The results demonstrate the capability of the method to provide physical insight into work produced by a transonic compressor rotor.

Keywords

Turbomachinery; Shock Buffet; Exergy; Large Eddy Simulation

NOMENCLATURE

Symbols

$\mathcal{A}_{[]}$	anergy quantity	W
C	chord length	m
$d\mathcal{S}_B$	blade surface area	m^2
$d\mathcal{S}_{CVB}$	control volume boundary integral surface area	m^2
$d\mathcal{V}$	control volume integral volume	m^3
e	specific internal energy	Jkg^{-1}
∞	freestream value	
$\mathcal{K}$	thermal conductivity	$Wm^{-1}K^{-1}$
$\hat{n}$	normal vector	
p_g	gauge pressure	Pa
ρ	density	kgm^{-3}
S	blade pitch	m
s	specific entropy	$Jkg^{-1}K^{-1}$
$\bar{\bar{\tau}}$	fluid shear stress tensor	Pa
T	temperature	K
V	velocity in the absolute reference frame	ms^{-1}
V'	velocity in the relative reference frame	ms^{-1}
$\mathcal{X}_{[]}$	exergy quantity	W

Abbreviations

ARF	absolute reference frame
DOF	degrees of freedom
$\mathcal{PER}$	potential for energy recovery
RRF	relative reference frame
SBLI	shock boundary layer interaction

1. INTRODUCTION

Modern transonic axial compressor rotors are optimised for high stage loading. The high loading is achieved through raising the relative inflow Mach number to be at supersonic conditions. This supersonic inflow results in a complex shock structure, originating as a bow-wave which extends into the passage between neighbouring blades. This bow shock delivers a large static pressure increase over a very short streamwise distance, therefore permitting static pressure ratios which would be unobtainable for a subsonic rotor design [1].

Although the shock offers a large pressure rise, it carries considerable disadvantages with regard to aeroelastic response and thermodynamic losses. As the bow shock extends into the passage it intersects

CC BY 4.0

doi: 10.25967/680053

with the suction side of the neighbouring rotor blade, where it encounters the boundary layer.
At Reynolds numbers typical of a compressor rotor operation, the boundary layer up to the intersection location is laminar or in a transitional state. The pressure gradient imposed by the shock results in the formation of a separation bubble and a rapid transition to turbulence downstream of the shock. This shock boundary layer interaction (SBLI) therefore determines the state of the boundary layer over the blade portion downstream of the shock, and at off-design conditions may result in complete boundary layer separation.
Furthermore, it is important to understand that this interaction is not steady and that the position of the shock's intersection point and the size of the separation region at any point in time are strongly coupled. In notable pieces of work to investigate SBLI in transonic axial compressor stages, high fidelity simulations were conducted on this by Klose et al. [2] and Munoz Lopez et al. [3] using the German Aerospace Center's TCTA transonic compressor profile. Their findings showed that the turbulence at the trailing edge of the blade induces pressure waves which travel upstream and intersect with the shock causing it to periodically oscillate, a phenomenon known as transonic buffet.
The impact of buffet for a compressor rotor is dependent on the shock oscillation frequency. On a rigid blade the oscillation is purely an aerodynamic instability, but when considering the presence of a blade's structure, the fluctuating surface pressures produce a periodic forcing on the structure. When the oscillation of the shock approaches the natural frequency of the blade structure, the shock motion can synchronise with the blade vibration in a locked-in state [4], in which the unsteady loading is phased with the blade displacement. Under certain conditions the net work done by the flow on the structure over an oscillation cycle then becomes positive, resulting in a self-excited oscillation of increasing amplitude known as flutter [5]. Although this phenomenon has been extensively explored for external aerodynamics [6], comparatively little work has addressed it in turbomachinery.
The aeroelastic consequences of the passage shock are also accompanied by a thermodynamic one. Although the shock is effective for creating a sharp increase in static pressure, it also results in an increase in entropy generation across the shock. Additionally, the highly turbulent and separated boundary layer region behind the shock leads to the dissipation of mechanical energy into internal energy through the action of viscosity. It is to be noted, however, that not all not all of the potential usability of the energy is immediately destroyed at the point of generation: the turbulent kinetic energy and wake non-uniformity remain out of equilibrium with the thermodynamic dead state and hence remain available to do work until the energy cascade and molecular transport have brought the flow to equilibrium.
These losses are not simply a by-product which must be accepted, instead they serve as a key metric against which any measure to control shock oscillations must be compared. A shock control bump for instance has potential to dampen shock oscillations but in doing so changes the strength and position of the shock, thickens the boundary layer passing over it and changes the separation region downstream of the bump and the shock. It is therefore important to not only consider any shock control device's ability to mitigate shock motion and flutter, but any study must also aim to understand the changes to thermodynamic losses and the form in which these losses occur. Conventional turbomachinery loss metrics, such as total pressure loss coefficients and isentropic efficiency [7], are poorly suited for quantifying the form and formation points of the losses, as integral measures evaluated between the inflow and outflow boundaries only report the result of all the combined mechanisms but not the composition of the losses.
The second law of thermodynamics based far-field analysis method offers a means of obtaining this decomposition. Formulated by Arntz et al. [8, 9], rather than just accounting for the flow of energy on its own, the method instead tracks the available work in the flow, distinguishing between exergy (the portion of energy that is still potentially available to do useful work relative to the thermodynamic dead state), and anergy (the portion of energy that has been irreversibly destroyed). Furthermore, both contributions can be decomposed by mechanism. The anergy ($\dot{\mathcal{A}}$) is decomposed into the portions destroyed by viscous dissipation, by thermal mixing, and across shock waves. The exergy ($\dot{\mathcal{X}}$) separates into the mechanical and thermal components which remain available to do useful work on entering the next blade row.
To date, application of the exergy balance to axial compressor rotors has been limited to steady-state Reynolds-averaged Navier-Stokes simulations, with turbulence modelling assumptions [10, 11], hence restricting the analysis to a time-averaged quantification of the losses. As the SBLI is inherently unsteady, resolving where and when the exergy is destroyed over a cycle of shock motion requires a scale-resolving simulation approach.
The objectives of this paper are threefold. Firstly the work aims to establish a scale resolving simulation methodology for a transonic compressor blade section and to characterise the unsteady behaviour of the passage shock and the resulting SBLI. Secondly, to apply the exergy balance to the resulting data, decomposing the losses into their reversible and irreversible components and attributing them to the physical mechanisms and locations within the passage where they are generated. Finally, to establish a rigid blade as the reference configuration against which subsequent research on flow control measures will be compared as a part of the SAFUMA research program, with the broader aim to investigate the mitigation of flutter in transonic compressor rotors through passive means. The present study does not

CC BY 4.0

investigate flutter directly, but establishes the aerodynamic and thermodynamic baseline against which future flutter-suppression concepts will be evaluated.

2. METHODOLOGY

2.1. Test Case

The test case is derived from the NASA Rotor 67 transonic compressor [12–15]. Rotor 67 is a first-stage transonic fan designed and tested at NASA Lewis Research Center in the 1980s. It is a 22 blade rotor with a design rotational speed of 16043 RPM. Due to the plethora of experimental data on the position of the passage shock at different flow conditions, the rotor has become a widely used test case for evaluating CFD solvers and has also become a prevalent test case for the study of aeroelasticity and compressor blade flutter analyses [16–18].
To isolate the shock buffet mechanism from the influence of span wise effects the investigation is carried out on a 2.5D section of a rotor blade. The section is taken at the 70% span (measured from the hub), which lies sufficiently far from the tip to avoid the influence of a tip leak vortex while still providing a relative inflow Mach number at which a strong passage shock is established. The station is also representative of the spanwise region in which aeroelastic flutter effects are expected to be prevalent for later studies based on the work established.

2.2. Numerical Set up

The study is conducted using the open-source GPU accelerated Discontinuous Galerkin Spectral Element solver GALÆXI [19, 20]. The flow is governed by the compressible Navier-Stokes equations, expressed in conservative form as:

$$\frac{\partial \mathbf{U}}{\partial t} + \nabla \cdot (\mathbf{F}^c(\mathbf{U}) - \mathbf{F}^v(\mathbf{U}, \nabla \mathbf{U})) = \mathbf{0}, \tag{1}$$

where $\mathbf{U}$ is the vector of conserved variables, while $\mathbf{F}^c$ and $\mathbf{F}^v$ denote the convective and viscous fluxes respectively. The system uses the ideal gas equation of state, with the dynamic viscosity evaluated using Sutherland's law. The simulation uses an implicit large eddy simulation (ILES) approach, where no sub-grid scale model is utilised; instead the spatial discretisation's numerical dissipation acts in place of an explicit closure.
The spatial discretisation is handled using an kinetic-energy-preserving split-form DG formulation [21], with a Legendre-Gauss-Lobatto node structure within the mesh elements, while the fluxes are calculated using Roe's approximate Riemann solver with entropy corrections. Time stepping is handled via an explicit low-storage 4th-order accurate Runge-Kutta time discretisation approach with the time step size constrained to match $\mathrm{CFL} = 0.9$. To ensure stability and accurate shock capturing the solver is set up to use the Perrson indicator to mark mesh elements with a troubled solution. The marked cells are then transformed to equidistant finite volume subcells with a TVD scheme avoiding the need for artificial viscosity [22].
To ensure adequate resolution for a wall-resolved simulation with polynomial order $N = 3$, the computational grid's near wall resolution is designed to target a $y^+ \approx 1$ with DOF-wise spacings $\Delta x^+ \approx 50$ and $\Delta z^+ \approx 20$. The computational domain shown in Figure 1 is extruded in the z direction to a thickness of 5% of the chord length (C), with periodic boundary conditions assigned to the spanwise extents. Overall, the computational grid contains ≈ 60 million DOF.

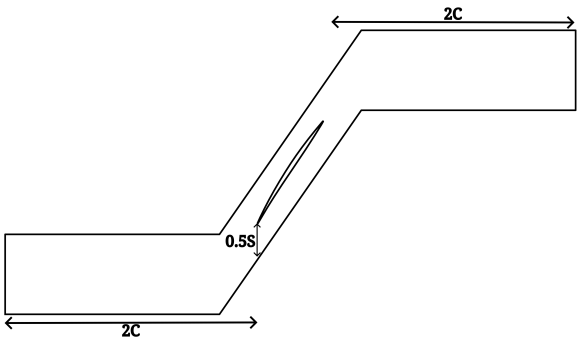


FIG 1. Computational domain
$C = 0.0987\,\mathrm{m}$ **and** $S = 0.05902\,\mathrm{m}$

The blade surface is assigned an adiabatic no-slip wall boundary condition, and is positioned in the middle of the domain with periodic boundary conditions at a distance of half the blade pitch above and below the chord line. The outflow boundary condition is set as a pressure outflow with $p_{\mathrm{stat}} = 132500\,\mathrm{Pa}$. The inflow is a Dirichlet boundary with conditions prescribed as shown in Table 1.

TAB 1. Inflow Boundary Conditions

Relative Reference Frame			
$\rho_\infty[kgm^{-3}]$	$V'_{x\infty}[ms^{-1}]$	$V'_{y\infty}[ms^{-1}]$	$p_{stat}[Pa]$
1.02873	197.15	347.19	79393.7
Absolute Reference Frame			
$\rho_\infty[kgm^{-3}]$	$V_{x\infty}[ms^{-1}]$	$V_{y\infty}[ms^{-1}]$	$p_{stat}[Pa]$
1.02873	197.15	0	79393.7

The simulation is run at a near-stall like operating condition, with the presented relative reference frame freestream conditions corresponding to $\mathrm{M}_{in} = 1.21$ and $Re = 2.2 \cdot 10^6$. It should be noted that the back pressure required to establish the passage shock in the present configuration is higher than that of a three-dimensional rotor at the same conditions [23]. The boundary conditions in Table 1 were selected

CC BY 4.0

through a parametric study to match the shock positions reported in Wood et al. [14].

2.3. Exergy Balance Implementation

As mentioned in the introduction, the exergy balance was originally developed by Arntz et al. [8, 9], where it is applied on a control volume fixed to the body and hence calculates its quantities in relation to the RRF. Subsequent work on the topic has instead adopted the usage of the ARF [24–26], in which the balance preserves the physical directionality of the process and hence allows for a more intuitive understanding of work done by the body. As such the work here presents the balance applied in the ARF, where the transformation is achieved through subtracting the speed of the blade ($V_{y\infty}$) from the obtained DOF local velocities.
In the present test case the near-field side of the balance is simplified in that it does not need to include source terms or the term to represent a moving geometry. The far-field balance used in the study is presented in equation 2, where the near-field body power is calculated as shown in equation 3.

$$\overbrace{-F_B \cdot U}^{\text{Near-Field}} = \overbrace{\dot{\mathcal{X}}_{v(t)} + \dot{\mathcal{X}}_{th} + \dot{\mathcal{X}}_m + \dot{\mathcal{A}}_\Phi + \dot{\mathcal{A}}_{\nabla T}}^{\text{Far-Field}} \tag{2}$$

$$-\mathbf{F_B} \cdot \mathbf{U} = \iint (p_g \mathbf{V}_\infty - \bar{\bar{\tau}} \cdot \mathbf{V}_\infty) \cdot d\mathcal{S}_\mathcal{B} \tag{3}$$

As the exergy components of the balance are inherently dependent on thermodynamic state of the fluid relative to the dead state, it is first necessary to calculate the specific static exergy of the fluid at each DOF as given in equation 4.

$$\mathcal{X}_s = (e - e_\infty) - T_\infty (s - s_\infty) + p_\infty \left(\frac{1}{\rho} - \frac{1}{\rho_\infty}\right) \tag{4}$$

The term $\dot{\mathcal{X}}_{v(t)}$ represents the rate of change of the exergy contained in the control volume. It consists of two contributions: $\dot{\mathcal{X}}_{ke}$, the rate of change of kinetic energy, and $\dot{\mathcal{X}}_s$, the rate of change of the static exergy of the fluid in the control volume.

$$\dot{\mathcal{X}}_{v(t)} = \underbrace{\frac{d}{dt} \iiint \left(\frac{\mathbf{V}^2}{2}\rho\right) d\mathcal{V}}_{\dot{\mathcal{X}}_{\text{ke}}} + \underbrace{\frac{d}{dt} \iiint \rho \mathcal{X}_s d\mathcal{V}}_{\dot{\mathcal{X}}_s} \tag{5}$$

$\dot{\mathcal{X}}_{th}$ represents the amount of static exergy flux across the boundaries of the control volume at an instantaneous point in time.

$$\dot{\mathcal{X}}_{th} = \iint \rho \mathcal{X}_s \mathbf{V}' \cdot d\mathcal{S}_{\mathcal{CVB}} \tag{6}$$

$\dot{\mathcal{X}}_m$ is the corresponding flux to the mechanical exergy transfer across the control volume boundaries. The mechanical exergy flux can be further decomposed into the transport of kinetic energy across the boundary ($\dot{\mathcal{E}}_k$), work done by pressure ($\dot{\mathcal{E}}_p$), and the work done by viscous stresses ($\dot{\mathcal{E}}_\tau$).

$$\dot{\mathcal{X}}_m = \underbrace{\iint \frac{\rho V^2}{2} \mathbf{V}' \cdot \mathrm{d}\mathcal{S}_{\mathcal{CVB}}}_{\dot{\mathcal{E}}_k} + \underbrace{\iint p_g \mathbf{V} \cdot \mathrm{d}\mathcal{S}_{\mathcal{CVB}}}_{\dot{\mathcal{E}}_p} - \underbrace{\iint \bar{\bar{\boldsymbol{\tau}}} \cdot \mathbf{V} \cdot \mathrm{d}\mathcal{S}_{\mathcal{CVB}}}_{\dot{\mathcal{E}}_\tau} \tag{7}$$

The two remaining terms account for the energy irreversibly destroyed within the control volume. Equation 8 calculates the anergy generated through viscous dissipation ($\dot{\mathcal{A}}_\Phi$), additionally the term is scaled by the DOF-local temperature ratio to account for local entropy production.

$$\dot{\mathcal{A}}_\Phi = \iiint \frac{T_\infty}{T} (\bar{\bar{\tau}} : \nabla V) d\mathcal{V} \tag{8}$$

$\dot{\mathcal{A}}_{\nabla T}$ is the anergy generated via thermal mixing, arising from the conduction of heat across temperature gradients.

$$\dot{\mathcal{A}}_{\nabla T} = \iiint T_\infty \mathcal{K} \left(\frac{\nabla T}{T}\right)^2 d\mathcal{V} \tag{9}$$

Additionally, Lamprakis et al. [24] showed that the exergy and anergy can be combined into a metric named the potential for energy recovery ($\mathcal{PER}$), as shown in equation 10.

$$\mathcal{PER} = 1 - \frac{\dot{\mathcal{A}}_\Phi + \dot{\mathcal{A}}_{\nabla T}}{\dot{\mathcal{X}}_{v(t)} + \dot{\mathcal{X}}_{th} + \dot{\mathcal{X}}_m + \dot{\mathcal{A}}_\Phi + \dot{\mathcal{A}}_{\nabla T}} \tag{10}$$

The $\mathcal{PER}$ is not a measure of the quantity of work supplied to the fluid but is rather a measure of the the quality of the work, expressing the fraction which has not been irreversibly destroyed and therefore remains theoretically available to produce useful work. The metric therefore allows for a rapid comparison between design variations and for an assessment of how changes may impact the blade rows and additional stages downstream of the control volume.
All exergy and anergy quantities reported in the results section are non-dimensionalised as shown in equation 11.

$$C_{()} = \frac{()}{\frac{1}{2}\rho_\infty V_\infty^3 S_B} \tag{11}$$

CC BY 4.0

Figure 2 shows how the control volume is positioned within the computational domain. The solid black lines represent the upper and lower periodic boundaries, which contribute nothing to the net balance as the flux exiting one is recovered at the other. The dashed lines denote the upstream and downstream boundaries of the control volume on which the flux quantities are calculated, whilst the volume integrals are calculated for the region between the dashed lines. As the rotor blade in this test case features a bow shock which extends across the upstream plane, the fluid travelling across the plane is not at equilibrium, and as such the front plane must be included in the balance calculations.

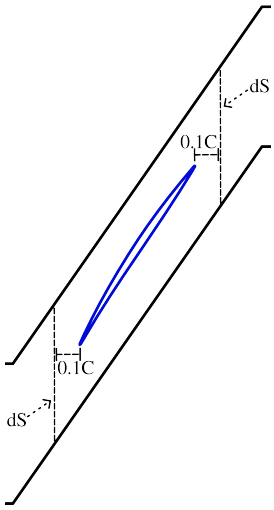


FIG 2. Control Volume Diagram (Not to Scale)

As the study focused on the changes through the blade passage, the boundaries were placed $0.1\mathrm{C}$ upstream and downstream of the leading and trailing edges respectively. The control volume is not restricted to a single fixed region as shown in the diagram, at selected time steps the downstream boundary is swept from the leading edge to the trailing edge, and the balance is evaluated at each sub-volume point. This allows for obtaining the result of the balance as a function of position, hence allowing for pinpointing where individual loss formations originate from and how they develop as you travel further over the blade's surface.

For the purposes of this work the balance is evaluated as a post-processing operation where the solution is first transformed to a 100% FV sub-cell solution. This is necessary as the boundaries of the arbitrary control volume do not generally align with the unstructured element boundaries of the DG mesh. A high-order element carries a single polynomial representation across its whole extent, and cannot be trivially divided at an arbitrary station without violating conservation, but the transformation to FV allows for both maintaining conservation and sweeping through the passage. The gradient quantities required by the anergy terms are evaluated on the high-order DG solution prior to the transformation, such that the impact on the dissipation and conduction terms is minimised. The cost of this approach is that the piecewise-constant subcell representation does not retain the full high-order information for calculation of the flux quantities, a method which evaluates the balance directly on the high order solution is the subject of ongoing development.

3. RESULTS

3.1. Time Averaged Results

As the present work is entirely a numerical study, checks are performed to ensure the near wall mesh quality meets the required targets and a check is performed on the obtained surface forces to ensure the simulation has exited the transient noise phase.

The near-wall resolution was assessed from the time-averaged wall units. Figure 3 shows the distribution of y^+ along the suction and pressure surfaces, while the corresponding surface- and time-averaged values of y^+, Δx^+ and Δz^+ are given in Table 2. The dimensional spacings used for calculating the values are estimated through assuming a equidistant node spacing within the cell.

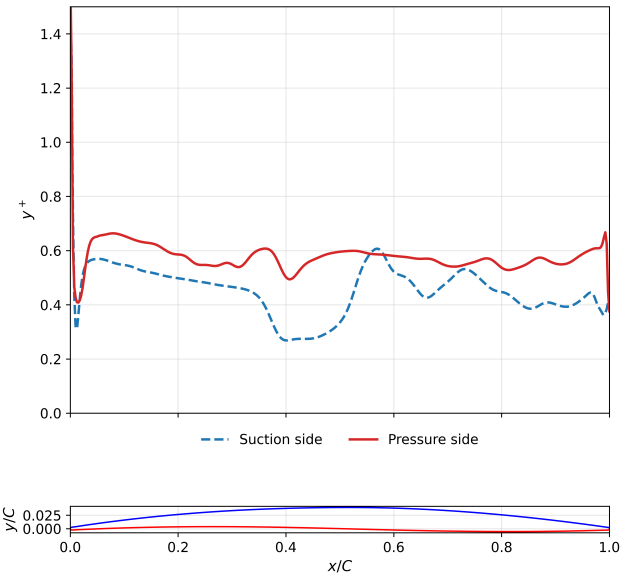


FIG 3. y^+ Distribution Over the Blade Surfaces

TAB 2. Spatially and Temporally Averaged Near Wall Resolution

y^+	Δx^+	Δz^+
0.51	41	22

It is seen that the values meet the targets for a wall-resolved simulation. It should be noted that the values are not calculated based on element size but are instead evaluated using the positional information of the DG solution nodes. Of note is a large reduction in the obtained y^+ value on the suction side

CC BY 4.0

of the blade between $\approx 0.4x/C$ and 0.55, indicating a sudden reduction in the wall shear stresses and therefore a substantial change in the boundary layer state, such as a sudden growth or separation bubble. The presence of a separation region is confirmed by the time-averaged skin friction coefficient (C_f) shown in Figure 4. On the suction surface the skin friction falls to near zero from $x/C \approx 0.4$, indicating a boundary layer close to separation over this region, which accounts for the corresponding reduction in y^+. A region of genuinely reversed flow follows, with C_f reaching a minimum of approximately -0.0018 near $x/C \approx 0.55$, before recovering to positive values by $x/C \approx 0.7$ as the flow reattaches.

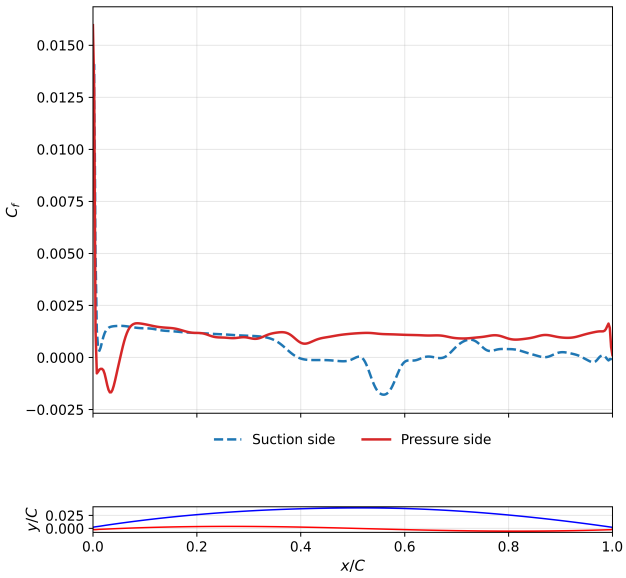


FIG 4. C_f Distribution Over the Blade Surfaces

Figure 5 shows the work done on the fluid by the rotor over time, calculated as given in equation 3. As the quantity is the scalar product of force and velocity, it accounts for all components of the surface force and therefore provides a single measure with which the decay of the initial transient start-up noise can be confirmed. The signal is seen to settle at $\mathrm{T/CTU} = 20$, where 1 $CTU = C/V_\infty$ with oscillation about a constant mean of $C_{\dot{W}} = 0.1748$.

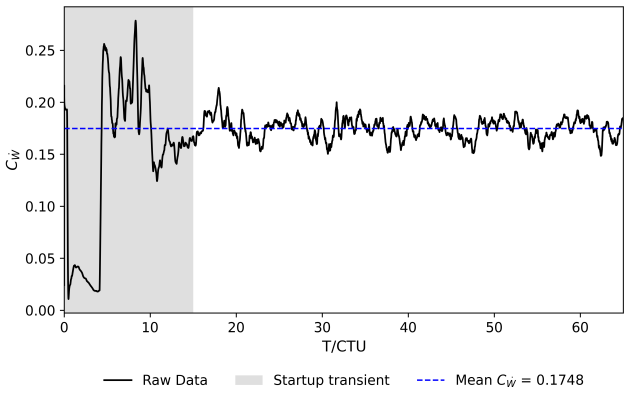


FIG 5. Work Done by the Blade over Time

3.2. Transient Flow Behaviour

To analyse the transient behaviour of the flow, a spectral analysis is done of the work done by the blade. The signal used to perform the Fast Fourier Transform (FFT) is taken from between $\mathrm{T/CTU} = 20$ and $\mathrm{T/CTU} = 67$. The signal is processed using Hann windows of $0.0003\mathrm{s}$ to suppress the influence of high frequency turbulent content, this is done purely for visualisation, as the FFT is still applied to the raw data. The signal is shown in Figure 6 wherein the smoothed data is identified on the raw data.

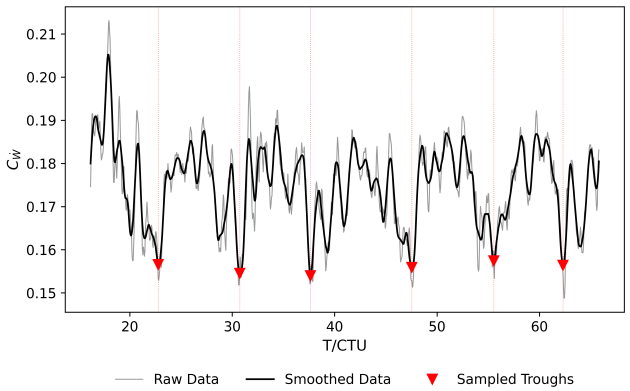


FIG 6. Filtered work signal used for the FFT.

A repeating pattern of troughs is apparent in the smoothed signal, with six identified across the analysis window at an approximately constant spacing of $8\,\mathrm{CTU}$. The power spectral density of the raw signal, shown in Figure 7, confirms this as a discrete tone. The discrete tone is identified at a frequency of $489\,\mathrm{Hz}$ and additionally a secondary peak can be seen at the first harmonic frequency ($2f$) of the discrete tone. It is important to note this peak at $489\,\mathrm{Hz}$ corresponds well with the established spacing between troughs in $C_{\dot{W}}$ signal.

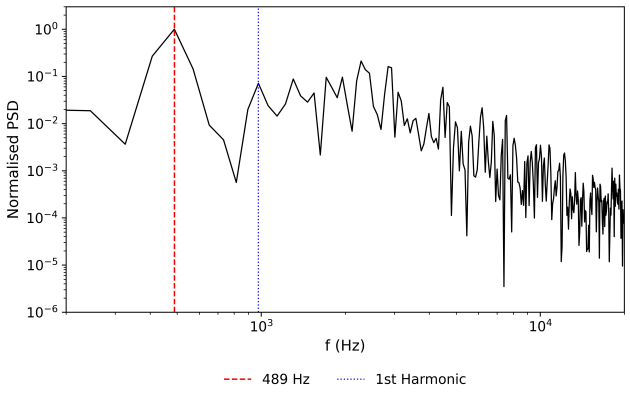
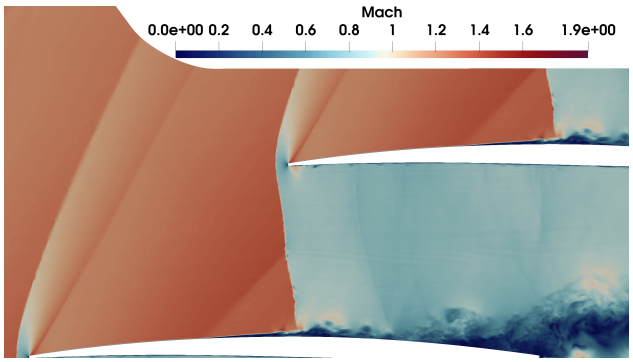


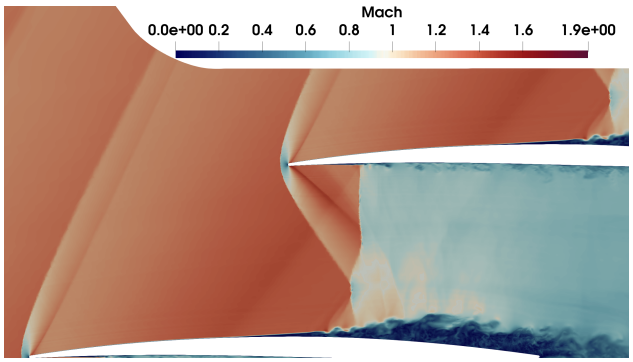
FIG 7. PSD Analysis of Blade Work.

To determine whether the dominant frequency arises from shock buffet and the associated STBLI, instantaneous Mach number contours in the blade passage were extracted at instants corresponding to two successive troughs in the $C_{\dot{W}}$ signal (Figures 8a and 8c), and at a time midway between the two troughs (Figure 8b).

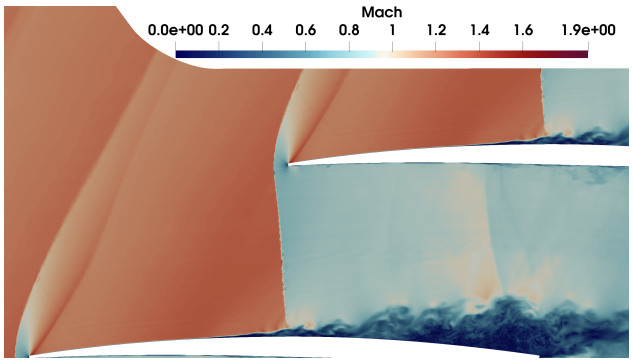
CC BY 4.0



(a) $\mathrm{T/CTU} = 47.54$



(b) $\mathrm{T/CTU} = 51.54$



(c) $\mathrm{T/CTU} = 55.54$

FIG 8. Instantaneous Mach Contours Showing Shock Position
(Blade orientation rotated in post processing for easier visibility)

At both trough instants, shown in Figures 8a and 8c, the shock is located at its most forward position, close to the leading edge of the upper blade in the passage, as is characteristic of near-stall condition and consistent with the near-stall shock position measured by Strazisar et al. [15]. At the time point between the two troughs (Figure 8b), the shock has moved downstream deeper into the passage, and its shock structure has changed. Rather than being a single shock structure it now features a lambda structure with a split of the shock intersecting with the pressure side of the upper blade in the passage. This change in structure is significant, as it implies the changes in $C_{\dot{W}}$ are not only attributed to the shock's motion but also to its change in structure.
The $C_{\dot{W}}$ signal registers that the work done on the fluid varies over the cycle, but it reports only the net quantity at each instant and cannot indicate the form the variation takes. Whether the change in work done by the blade at the rear position reflects a change in the entropy formation across the shock, or takes the form of another energy wastage, cannot be identified only with near-field metrics.

3.3. Exergy Analysis

The balance is first evaluated at the two extremes of the shock oscillation, comparing the instant at which the shock lies at its most forward position ($\mathrm{T/CTU} = 47.54$), with when it lies furthest into the passage ($\mathrm{T/CTU} = 51.54$).
Before decomposing the work done, the far-field and near-field sides of the balance are compared at both instants to quantify the imbalance present. As the two sides are evaluated independently, the agreement between them provides a direct check on the implementation of the balance, and any error introduced through the effects of distance between integration points and from the 100% FV conversion step. The comparison is seen in Table 3.

TAB 3. Balance Accuracy Comparison

T/CTU	Near-Field $C_{\dot{W}}$	Far-Field $C_{\dot{W}}$	% Diff
47.54	0.1518	0.1573	3.615
51.54	0.1805	0.1869	3.591

At both time instants the far-field portion of the balance agrees with the near-field with an imbalance of roughly 3.6%. The consistency of the discrepancy between the two shock positions indicates a systematic error rather than a phase-dependent error source. The agreement is considered sufficient for the decomposition presented below.

TAB 4. Flow-field Decomposition

T/CTU	$C_{\dot{\mathcal{X}}_{v(t)}}$	$C_{\dot{\mathcal{X}}_m}$	$C_{\dot{\mathcal{X}}_{th}}$	$C_{\dot{A}_\Phi}$	$C_{\dot{A}_{\nabla T}}$
47.54	−0.0064	0.1438	0.0165	0.0031	0.0003
51.54	−0.0037	0.1659	0.0218	0.0027	0.0002

The decomposed balance at both instants is given in Table 4. At both shock positions the majority of the work supplied by the blade remains available as exergy, predominantly in mechanical form ($\dot{X}_m$). The mechanical exergy ($\dot{X}_m$) can be further decomposed into its base components as given in Equation 7. This is shown in Table 5.
The decomposition shows that the difference in work between the two shock positions is almost entirely attributable to the pressure term ($\mathcal{E}_P$), which increases from 0.0948 to 0.1162 as the shock moves rearward, while the kinetic contribution changes by less than 2%.
Overall, this distribution is consistent with the mode

CC BY 4.0

TAB 5. $\dot{\mathcal{X}}_m$ Decomposition

T/CTU	$C_{\dot{\mathcal{E}}_k}$	$C_{\dot{\mathcal{E}}_p}$	$C_{\dot{\mathcal{E}}_\tau}$
47.54	0.0489	0.0948	$-5.4 \cdot 10^{-7}$
51.54	0.0498	0.1162	$6.3 \cdot 10^{-8}$

of operation of the rotor. The work supplied by the blade appears predominantly as pressure work, with a smaller kinetic contribution imparted to the flow. The total percentage of theoretically recoverable energy leaving the passage at this control volume boundary towards the next blade row and stages can be expressed as the PER.

Evaluating Equation 10 at the two instants gives $\mathrm{PER} = 0.978$ when the shock lies at its forward position and $\mathrm{PER} = 0.985$ when it lies within the passage. The lower value at the forward position is consistent with the stronger, more normal shock structure observed there, though the difference between the two is small. In both cases, the value confirms that, at a station immediately downstream of the trailing edge, almost all of the work supplied by the blade remains theoretically available to the following blade row. Although this may appear to suggest that the shock introduces little in the way of irreversible losses, such a conclusion would be incorrect. The downstream boundary of the control volume lies immediately behind the trailing edge of the blade. The turbulent kinetic energy generated in the separated shear layer, and the velocity and thermal non-uniformity of the wake, have therefore had little opportunity to dissipate and remain out of equilibrium with the dead state at the measurement station.

To demonstrate how the balance may be evaluated through the passage, the control volume is swept from the leading edge to the trailing edge, with the balance re-evaluated at each station. This is shown for the forward shock position in Figure 9.

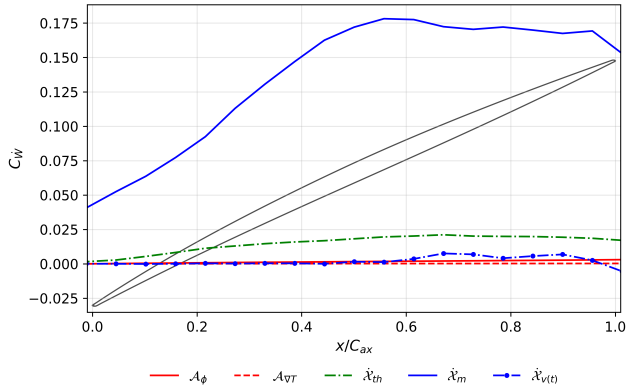


FIG 9. Sweep Through Blade Passage at $T/\mathrm{CTU} = 47.54$

The results show the development of the individual terms through the passage. The mechanical exergy $\dot{\mathcal{X}}_m$ rises steeply over the forward portion of the blade as work is delivered to the fluid, but does not continue to increase through the full passage. It reaches a maximum at approximately $x/C_{ax} = 0.57$ and thereafter declines towards the trailing edge. The thermal exergy flux $\dot{\mathcal{X}}_{th}$ follows a similar trend at an order of magnitude smaller, and the anergy terms remain small throughout, accumulating gradually rather than at any single station. Of particular note is the coincidence between the onset of the decline in $\dot{\mathcal{X}}_m$ and the point at which the unsteady storage term $\dot{\mathcal{X}}_{v(t)}$ departs from zero and begins to fluctuate, at approximately $x/C_{ax} = 0.6$. This station corresponds closely to the location at which the passage shock meets the suction surface boundary layer, as observed in Figure 8a. The coincidence suggests that the onset of exergy-storage fluctuations and the decline in mechanical exergy are both linked to the shock induced turbulent transition of the boundary layer.

As Table 5 showed $\dot{\mathcal{X}}_m$ is the dominant form in which work is delivered to the fluid, and the term in which the largest difference between the two shock positions appears, its decomposition is also swept through the passage at both instants. This allows the effect of the shock position and structure on the formation of $\dot{\mathcal{X}}_m$ to be directly compared. The result is shown in Figure 10, where $\mathrm{T/CTU} = 47.54$ is represented by the solid line and $\mathrm{T/CTU} = 51.54$ represents the dashed lines.

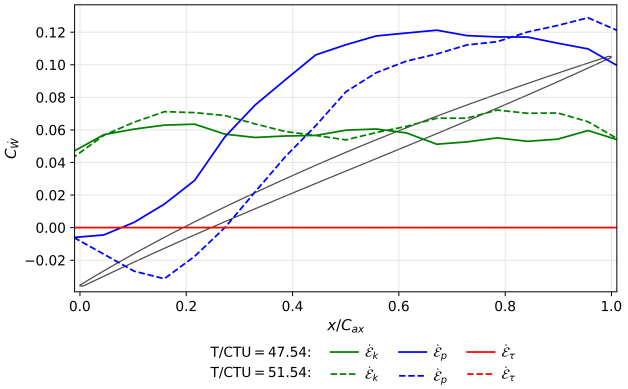


FIG 10. $\dot{\mathcal{X}}_m$ Sweep Through Blade Passage

Figure 10 shows the development of the components of $\dot{\mathcal{X}}_m$ through the passage at both instants. The viscous work term $\dot{\mathcal{E}}_\tau$ is negligible across the whole passage. The kinetic contribution $\dot{\mathcal{E}}_k$ is on average slightly higher when the shock lies further into the passage, though the difference is small in comparison with that in the pressure term, which carries the majority of the change between the two instants. The behaviour of $\dot{\mathcal{E}}_p$ differs markedly between the two positions. With the shock at its forward position, the pressure work rises steeply from the leading edge and reaches a plateau by approximately $x/C_{ax} = 0.6$, after which it declines towards the trailing edge. With the shock further into the passage ($\mathrm{T/CTU} = 51.54$), the pressure work is initially lower, falling to a minimum near $x/C_{ax} = 0.18$ before rising, but continues to increase over the whole passage without reaching a plateau. The consequence is that although the rearward shock

CC BY 4.0

position yields the lower pressure work over the forward portion of the blade, the sustained rise allows it to exceed the total work produced once the flow has travelled through the entire passage.

4. CONCLUSION

This work has demonstrated the application of the far-field exergy balance to a scale-resolving simulation of a 2.5D transonic compressor blade section. The work done on the fluid by the blade was found to fluctuate at a discrete frequency of $489\,\mathrm{Hz}$. Instantaneous Mach number contours extracted at successive troughs and at the intervening maximum confirmed that this frequency corresponds to the oscillation of the passage shock, which traverses between a forward position characteristic of near-stall operation and a rearward position within the passage, changing structure as it does so to closer resemble the shock system associated with peak-efficiency operation. The fluctuations in total work are therefore directly attributable to the motion and reconfiguration of the shock and its interaction with the blade surface's boundary layer.

The exergy balance was then applied at the two extrema of the shock oscillation. The far-field and near-field sides of the balance were found to agree to approximately 3.6% at both instants. The decomposition showed that the majority of the work supplied by the blade remains available as mechanical exergy at a station immediately downstream of the trailing edge, with the destroyed exergy amounting to between 1.5 and 2.2% of the total, corresponding to a $\mathcal{PER}$ of 0.978 and 0.985 at the forward and rearward shock positions respectively.

Finally, it was demonstrated that the balance can be swept through the passage to resolve the development of each contribution with axial position. This identified the station at which the unsteady storage term $\dot{\mathcal{X}}_{v(t)}$ first departs from zero, coinciding closely with the location at which the shock meets the boundary layer, and allowed the difference in work between the two shock states to be attributed to the pressure work term and quantified as a function of position through the passage.

The methodology established here provides the basis on which the effect of passive flow control devices, and specifically shock control bumps, may be assessed within the SAFUMA program. Two areas for further development have been identified in the course of this work. The first is the evaluation of the balance directly on the high-order DG representation, rather than through the transformation of the solution to a finite volume form as required here. The second is the application of the balance within a moving mesh framework, which would permit its use in flutter-driven fluid-structure interaction studies. Within the turbomachinery environment this would require an adaptation to the implementation to account for the presence of phase shifted periodic conditions required for flutter simulations.

ACKNOWLEDGEMENTS

The authors gratefully acknowledge the Federal Ministry for Economic Affairs and Energy (BMWE) for funding this work in the framework of the research project SaFuMa (FKZ: 20E2409). The research presented in this paper was funded in parts by the state of Baden-Württemberg under the project Aerospace 2050 MWK32-7531-49/13/7 "FLUTTER". The authors also gratefully acknowledge the support and the computing time on “Hunter” provided by the HLRS through the project “hpcdg”.

Contact address:

justin.du-plessis@iag.uni-stuttgart.de

References

[1] S. L. Dixon and C. A. Hall. *Fluid Mechanics and Thermodynamics of Turbomachinery*. Butterworth-Heinemann. DOI: https://doi.org/10.1016/C2011-0-05059-7.

[2] Bjoern F. Klose, Christian Morsbach, Michael Bergmann, Edwin J. Munoz Lopez, Alexander Hergt, and Edmund Kügeler. The unsteady shock–boundary layer interaction in a compressor cascade—part II: High-fidelity simulation. 147(9):091002. DOI: 10.1115/1.4067097.

[3] Edwin J. Munoz Lopez, Alexander Hergt, Joachim Klinner, Bjoern Klose, Chris Willert, and Volker Gümmer. The unsteady shock-boundary layer interaction in a compressor cascade—part III: Mechanisms of shock oscillation. 147(9):091003. DOI: 10.1115/1.4066186.

[4] Daniella E. Raveh. Numerical study of an oscillating airfoil in transonic buffeting flows. 47(3):505–515. DOI: 10.2514/1.35237.

[5] Earl H. Dowell, editor. *A Modern Course in Aeroelasticity*, volume 264 of *Solid Mechanics and Its Applications*. Springer International Publishing. ISBN: 978-3-030-74235-5 978-3-030-74236-2. DOI: 10.1007/978-3-030-74236-2.

[6] Nicholas F. Giannelis, Gareth A. Vio, and Oleg Levinski. A review of recent developments in the understanding of transonic shock buffet. 92:39–84. DOI: 10.1016/j.paerosci.2017.05.004.

[7] J. D. Denton. Loss mechanisms in turbomachines. volume Volume 2: Combustion and Fuels; Oil and Gas Applications; Cycle Innovations; Heat Transfer; Electric Power; Industrial and Cogeneration; Ceramics; Structures and Dynamics; Controls, Diagnostics and Instrumentation; IGTI Scholar Award of *Turbo Expo*, page V002T14A001, 05 1993. DOI: 10.1115/93-GT-435.

CC BY 4.0

[8] Aurélien Arntz, Olivier Atinault, and Alain Merlen. Exergy-based formulation for aircraft aeropropulsive performance assessment: Theoretical development. *AIAA Journal*, 53(6):1627–1639, 2015. DOI: 10.2514/1.J053467.

[9] Aurélien Arntz, Olivier Atinault, Daniel Destarac, and Alain Merlen. Exergy-based aircraft aeropropulsive performance assessment: CFD application to boundary layer ingestion. In *32nd AIAA Applied Aerodynamics Conference*. American Institute of Aeronautics and Astronautics. DOI: 10.2514/6.2014-2573.

[10] Ilyès Berhouni, Ilias Petropoulos, and Didier Bailly. Decomposition of compressible and thermal contributions to the exergy-balance-based analysis of the NASA rotor 37. In *Volume 12A: Turbomachinery — Axial Flow Fan and Compressor Aerodynamics*, page V12AT29A001. American Society of Mechanical Engineers. DOI: 10.1115/GT2024-120925.

[11] Jean-Christophe Boniface, Ilias Petropoulos, and Ilyès Berhouni. Exergy-based analysis of the NASA SDT configuration. In *Volume 12A: Turbomachinery — Axial Flow Fan and Compressor Aerodynamics*, page V12AT29A022. American Society of Mechanical Engineers. DOI: 10.1115/GT2024-125784.

[12] M. J. Pierzga and J. R. Wood. Investigation of the three-dimensional flow field within a transonic fan rotor: Experiment and analysis. 107(2):436–448. DOI: 10.1115/1.3239744.

[13] A. J. Strazisar. Investigation of flow phenomena in a transonic fan rotor using laser anemometry. 107(2):427–435. DOI: 10.1115/1.3239743.

[14] Jerry R Wood, Anthony J Strazisar, and P. Susan Simonyi. Shock stucture measured in a transonic fan using laser anemometry. In *AGARD Conference Proceedings No. 401 Transonic and Supersonic Phenomena in Turbomachines*, pages 2–1.

[15] J Strazisar, R Wood, D Hathaway, and L Suder. Laser anemometer measurements in a transonic axial-flow fan rotor.

[16] Meng-Sing Liou and Weigang Yao. Flutter analysis for turbomachinery using volterra series. In *Volume 7B: Structures and Dynamics*, page V07BT35A004. American Society of Mechanical Engineers. DOI: 10.1115/GT2014-25474.

[17] Jia Ren, Huang Huang, Dingxi Wang, Xu Dong, and Bochao Cao. An efficient coupled-mode flutter analysis method for turbomachinery. 106:106215. DOI: 10.1016/j.ast.2020.106215.

[18] R Wiranegara and A Turan. A simple approach to computational aeroelasticity of NASA rotor 67. In *ICAS 2014*, Germany, September 2014. International Council of the Aeronautical Sciences.

[19] Daniel Kempf, Marius Kurz, Marcel Blind, Patrick Kopper, Philipp Offenhäuser, Anna Schwarz, Spencer Starr, Jens Keim, and Andrea Beck. GALÆXI: Solving complex compressible flows with high-order discontinuous Galerkin methods on accelerator-based systems. *Computer Physics Communications*, 306, 2024. DOI: 10.1016/j.cpc.2024.109388.

[20] Spencer Starr, Yannik Feldner, Patrick Kopper, Marcel Blind, Daniel Kempf, Jannik Schrempp, Felix Rodach, Andrea Beck, and Anna Schwarz. An architecture-agnostic high-order discontinuous Galerkin framework for compressible flows, 2026.

[21] Sergio Pirozzoli. Numerical methods for high-speed flows. *Annual Review of Fluid Mechanics*, 43:163–194, 01 2011. DOI: 10.1146/annurev-fluid-122109-160718.

[22] Nico Krais, Andrea Beck, Thomas Bolemann, Hannes Frank, David Flad, Gregor Gassner, Florian Hindenlang, Malte Hoffmann, Thomas Kuhn, Matthias Sonntag, and Claus-Dieter Munz. FLEXI: A high order discontinuous Galerkin framework for hyperbolic-parabolic conservation laws. *Computers & Mathematics with Applications*, 81:186–219, 2021. DOI: https://doi.org/10.1016/j.camwa.2020.05.004.

[23] Spencer Starr, Anna Schwarz, Justin du Plessis, Andreas Wanninger, Johanna Hintz, Rohan Kaushik, Patrick Kopper, and Andrea Beck. APU-accelerated large eddy simulation with the discontinuous Galerkin solver GALÆXI, 2026.

[24] Ioannis Lamprakis, Drewan S. Sanders, and Panagiotis Laskaridis. Fundamental concepts of boundary-layer ingestion propulsion. *Journal of Aircraft*, 62(5):1182–1203, 2025. DOI: 10.2514/1.C037675.

[25] Justin du Plessis, Drewan Sanders, Tamas Józsa, and Tom-Robin Teschner. Far-field exergy-based drag decomposition of a turbulent blunt-body wake with hybrid-les. pages 254–259, 01 2026. DOI: 10.21741/9781644904251-45.

[26] Dameon Westley, Lelanie Smith, Drewan Sanders, Manuel Carreño Ruiz, and Domenic D'Ambrosio. Comparison of far-field methodologies for unsteady low reynolds number flows. pages 187–192, 01 2026. DOI: 10.21741/9781644904251-33.

CC BY 4.0